

Contents lists available at ScienceDirect

Journal of Physics and Chemistry of Solids

journal homepage: www.elsevier.com/locate/jpcs



Nb₂O₅ and Nb₁₀ nanocluster supported by TiO₂ rutile (110) surfaces: A co-catalyst for the enhanced reduction of NO molecules by first principle study

S. Muthukrishnan a,b, R. Vidya a,b,*, Anja Olafsen Sjåstad c

- a Centre for Materials Informatics (C-MaIn), Sir. C.V. Raman Science Block, Anna University, Sardar Patel Road, Guindy, Chennai, 600025, India
- b Computational Laboratory for Multifunctional Materials (CoLaMM), Department of Physics, Anna University, Sardar Patel Road, Guindy, Chennai, 600025, India
- ^c Centre for Materials Science and Nanotechnology, Department of Chemistry, University of Oslo, PO Box 1033, Blindern, N-0315, Oslo, Norway

ARTICLEINFO

Keywords:

Metal/metal oxide nanoclusters Surface chemical functionalization Nanocluster–surface interfaces NO adsorption and dissociation NO dissociation mechanism

ABSTRACT

Anthropogenic NO_x emissions from industrial sources pollute the Earth's atmosphere. It produces adverse effects on the Earth and human beings. TiO2 has the potential application for the photocatalytic degradation of environmental NO_x pollutants. Pure TiO₂ may have some practical limitations. Surface chemical functionalization of metal and metal oxide nanoclusters on top of the TiO2 surface may enhance photocatalytic activity toward reducing environmental NO_x pollution. Hence, we have presented a state-of-the-art Density functional theorybased study on the surface chemical functionalization of the transition metal oxide Nb₂O₅ and the metal Nb₁₀ nanocluster supported by TiO2 rutile (110) surfaces for the reduction of harmful environmental NO pollutants. The most favorable geometry and size of the Nb_2O_5/Nb_{10} nanocluster are studied. The binding energetics were analyzed to study the growth of Nb₂O₅/Nb₁₀ nanoclusters and their stability. The interaction and the charge transport between the nanocluster and the surfaces are studied by electronic structure, charge density, and the Bader charge analysis. Ab-Initio Molecular Dynamics (AIMD) analysis was carried out in order to study the thermodynamic stability of the nanocluster-supported TiO2 surfaces. The favorable adsorption sites of NO molecules on the Nb₂O₅/TiO₂ surface are studied by the adsorption energetics. From the Nb₂O₅/TiO₂ (Nb₁₀/ TiO2) surface, the dissociation of NO molecules into N, O by-products, and other harmless by-products is proposed by different possible mechanisms by reaction coordinates profile with the aid of Nudged Elastic Band methods. The transition state for the reaction mechanism is calculated. Our analysis will help understand the nature of the interaction between metal oxide/metal nanoclusters and oxide surfaces. A possible way to reduce the NO molecules through the novel oxide surfaces is proposed. Our theoretical analysis will provide a new pathway to reduce the environmental NO_x pollutants.

1. Introduction

The anthropogenic emission of NO_x produces adverse environmental effects, such as atmospheric air pollution, depletion of the ozone layer, acid rain, and global warming. In human beings, it affects the respiratory system, leading to breathing difficulties and issues [1–6]. Emissions from the industry and automobile vehicles are known as a common source of NO_x pollution [7–10]. Reducing this pollutant by the photocatalytic redox reaction is the most promising approach. TiO_2 has the potential capabilities for photocatalytic applications [11]. TiO_2 is regarded as the most hopeful semiconductor photocatalyst for its

advantages, such as being non-toxic, relatively cheap, chemically stable, and photo-stable. Also, it has been known that, among the various planes, TiO_2 Rutile (110) has the highest thermodynamic stability and lower surface energy; hence, it has the most technological applications [12]. Pure TiO_2 has a few disadvantages, such as a large band gap of about 3.0 eV [13]. This restricts its photo-catalytic activity only in the UV region of the solar spectrum. Also, the higher recombination of photo-generated electron and hole charge carriers greatly restricts the efficiency of photocatalytic redox reactions. By reducing the band gap of TiO_2 , it can perform the photocatalytic activity by visible light spectrum [14–18]. TiO_2 can be made into more efficient photocatalysts by doping

E-mail address: vidyar@annauniv.edu (R. Vidya).

^{*} Corresponding author. Centre for Materials Informatics (C-MaIn), Sir. C.V. Raman Science Block, Anna University, Sardar Patel Road, Guindy, Chennai, 600025, India.

external elements into it [19]. Even though doping is considered the most practical method, it has a few disadvantages. Such as the lack of stability of the host compound, recombination of the charge carriers, and issues in reproducibility, which are the adverse effects that reduce the photocatalytic activity [20–22]. Functionalizing the TiO_2 surfaces with metal nanoparticles opens the pathway to tune their electronic structure characteristics and also enhances their applications [23]. Noble metal functionalization on TiO_2 improves their photocatalytic applications toward visible light absorption. The deposition of noble metal nanoclusters such as Au, Ag, Pt, and Ru on other semiconductor surfaces gives improved photocatalytic properties, but the addition of noble metals is costly [24]. Exploring an efficient photocatalyst with cost-effectiveness will fulfill the practical necessity [25].

Semiconductor coupling is considered the most promising approach to modifying the physical-chemical properties of the oxide surfaces towards photocatalytic applications. Several previous study reports favorable evidence for tuning the oxide surfaces through semiconductor coupling. The interface of TiO2 with CdS gives better photoactivity towards visible light absorption. Interfacing the two semiconductors can be considered an advantage for photocatalytic activity by increasing the active sites for pollutants [26]. The surface modification of ZnGa₂O₄ with a SnO₂ semiconductor improves its photocatalytic activity towards the visible spectrum [27]. The deposition of oxide nanoclusters on top of the surface enhances the total surface area and thus improves the charge transport mechanism for the photocatalytic degradation of pollutant molecules. The interface of surfaces and deposited nanoclusters has low-coordinated sites on the surfaces, thus acting as binding sites for pollutant adsorption. The previous studies on transition metal oxide deposited TiO2 surfaces show efficient photocatalytic activity through enhanced charge carrier transport [28].

The deposition of iron oxide nanoclusters on top of the TiO₂ surface, show better efficiency by improving the optical absorption towards the visible spectrum and also reducing the recombination of electron and hole charge carriers [29]. The catalytic property of the oxide surfaces is greatly modified by the addition of a nanocluster on top of them. The stoichiometry termination. coordination. and size, nanocluster-supported TiO2 surfaces greatly influence the charge transport, and thus affect the photocatalytic activity [30]. Nb₂O₅ is a semiconductor with enormous scientific applications in the field of photocatalysts. Nb₂O₅ is cost-effective, chemically stable, and easily available [31-34]. Even though Nb₂O₅ can be used as a photocatalyst, the higher recombination of photo-generated charge carriers greatly restricts its activity. The coupling of Nb₂O₅ and TiO₂ leads to a superior photocatalyst by overcoming the drawbacks of pure compounds

In this work, we have shown the state-of-the-art Density functional theory-based study for the $\rm Nb_2O_5/Nb_{10}$ nanocluster supported by $\rm TiO_2$ rutile (110) surfaces for the enhanced reduction of harmful NO molecules. The growth of the nanoclusters and their stability can be studied by the binding energies. The interaction and the charge transport between the nanocluster and the surfaces are further studied by electronic structure, charge density, and the Bader charge analysis. The thermodynamic stability of the nanocluster-supported $\rm TiO_2$ surfaces was studied by Ab Initio Molecular dynamics (AIMD) analysis. The favorable adsorption sites of NO molecules on the Nanocluster/TiO_2 surface are studied by the adsorption energetics. The dissociation of NO molecules into N and O by-products is proposed by a different possible mechanism by reaction coordinates profile with the aid of transition state calculation.

2. Methodology

The Density Functional Theory calculations were done by localized atomic orbital basis set methods as programmed in the SIESTA packages [41,42]. The exchange-correlation functions were considered by Generalized Gradient Approximations (GGA), as by the Perdew, Burke,

and Ernzerhof formalism [43]. The core electrons were described by the Troullier-Martins-based pseudopotentials, and the valence electrons are depicted by a doubly ζ polarized basis set [44]. A mesh cutoff of about 300 Ry was used for the real-space integration. Monkhorst-Pack k-point mesh of a 4 \times 4 \times 1 and 2 \times 2 \times 1 was used for the Brillouin Zone integration for the electronic structure and the relaxation calculation, respectively. The convergence is achieved by setting the convergence threshold values as 10^{-6} eV and 0.05 eV/Å for energy and force, respectively. For the consideration of the slab model, a 4 \times 2 supercell of two layers of thickness was used, and a vacuum of 15 Å was implemented along the Z direction. The Nb₂O₅ nanocluster with different nanocluster sizes was modeled on the TiO2 Rutile (110) surfaces and further studied accordingly. For metal nanoclusters, the Nb₁₀ nanocluster is studied. During the geometry optimization, the bottom layers of the nanocluster/TiO₂ system are fixed, and the remaining layers are allowed to relax. The charge present on the surfaces is calculated by Bader charge analysis [45]. The transition state (TS) was calculated by the climbed-image nudged elastic band (CI-NEB) calculations [46]. VESTA packages were used for the visualization of crystal structure and electronic structure results [47].

3. Results and discussions

3.1. Binding energy and geometrical structure of Nb₂O₅/TiO₂

The initial stage is the optimization of isolated Nb₂O₅ nanoclusters. We modeled isolated forms of Nb₂O₅ nanoclusters with different nanocluster sizes, such as (Nb₂O₅)₁, (Nb₂O₅)₂, (Nb₂O₅)₃, and (Nb₂O₅)₄. Fig. 1 shows the geometrical structure of the (Nb₂O₅)₁, (Nb₂O₅)₂, (Nb₂O₅)₃, and (Nb₂O₅)₄ isolated nanoclusters in (a), (b), (c), and (d), respectively. The cohesive energy vs size of the nanocluster plots is shown in Fig. 1(e). Equation (1) is used to calculate the cohesive energy of the isolated nanocluster. Where $E_{(Nb_2O_5)n}$ is the total energy of the isolated Nb₂O₅ nanocluster, and $E_{(Nb_2O_5)}$ is the total energy of the isolated single Nb₂O₅ formula unit.

Hence, the calculated cohesive energy of isolated $(Nb_2O_5)_2$, $(Nb_2O_5)_3$, and $(Nb_2O_5)_4$ nanoclusters is -11.75 eV, -18.16 eV, and -25.10 eV, respectively. Here, the isolated $(Nb_2O_5)_4$ nanocluster has the highest cohesive energy; hence, it will be more stable than the other nanoclusters.

$$E_{C.E} = E_{(Nb2O5)n} - n X E_{(Nb2O5)}$$
 (1)

The TiO_2 Rutile (110) surfaces were modeled from the bulk TiO_2 Rutile unit cell. Fig. S1 in the supplementary materials shows the unit cell structure (a) and its projected density of states (b) for the TiO_2 Rutile unit cell. Fig. S2 in the supplementary materials shows the 4 \times 2 supercell structure (a), its projected density of states (b) for the TiO_2 Rutile (110) surface.

The optimization of the Nb_2O_5 nanocluster on top of the TiO_2 Rutile (110) surfaces is further studied. Hence, we modeled Nb_2O_5 nanocluster-supported TiO_2 surfaces with different nanocluster sizes, such as $(Nb_2O_5)_1$, $(Nb_2O_5)_2$, $(Nb_2O_5)_3$, and $(Nb_2O_5)_4$. Equation (2) is used to calculate the binding energy of the nanocluster decorated on the TiO_2 surface.

$$E_{B.E} = E_{(Nb2O5)n/TiO2} - E_{TiO2} - E_{(Nb2O5)n}$$
 (2)

Where $E_{(Nb2O5)n/TiO2}$ is the total energy of the Nb_2O_5 nanocluster-supported TiO_2 Rutile (110) surfaces, E_{TiO2} is the total energy of bare TiO_2 Rutile (110) surfaces, and $E_{(Nb2O5)n}$ is the total energy of isolated Nb_2O_5 nanoclusters. Based on that, the binding energy of the Nb_2O_5 nanocluster on TiO_2 with different cluster sizes is calculated accordingly Fig. 2. Hence, the binding energy of $(Nb_2O_5)_1/TiO_2$, $(Nb_2O_5)_2/TiO_2$, $(Nb_2O_5)_3/TiO_2$, and $(Nb_2O_5)_4/TiO_2$ nanoclusters is -3.40 eV, -3.57 eV, -4.47 eV, and -8.20 eV, respectively. Among the various models, $(Nb_2O_5)_4$ nanocluster-supported TiO_2 Rutile (110) surfaces have the

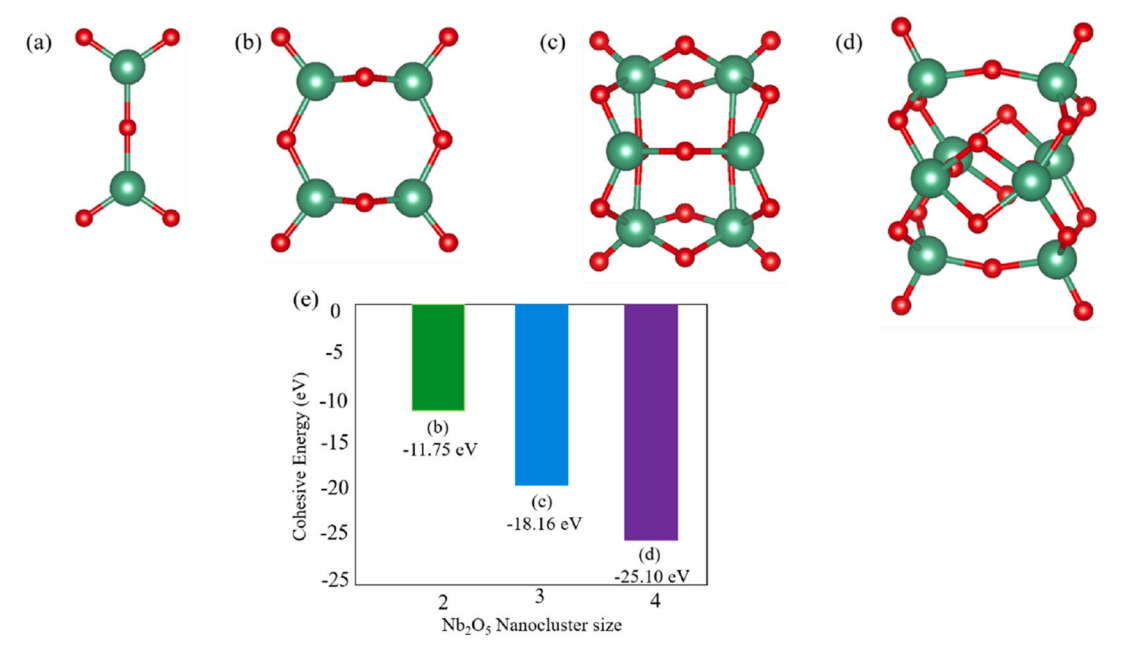


Fig. 1. The isolated Nb₂O₅ nanocluster with different nanocluster sizes (a, b, c, and d). Cohesive energy vs nanocluster size plots (e). Green and red balls represent the Nb and O atoms, respectively. (For interpretation of the references to colour in this figure legend, the reader is referred to the Web version of this article.)

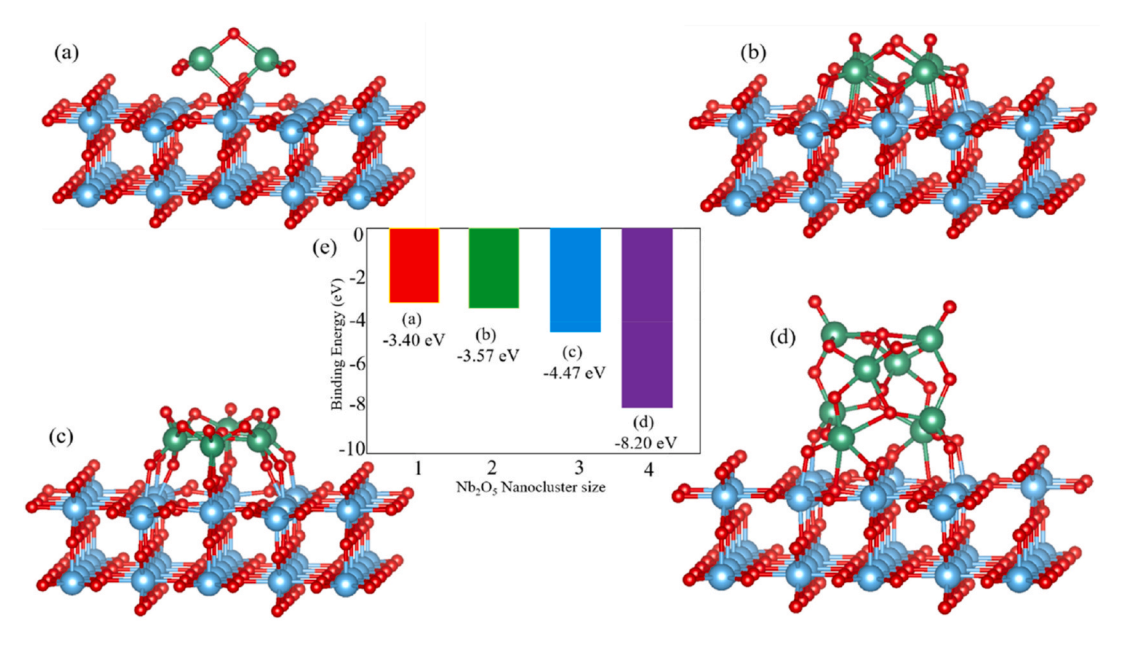


Fig. 2. The Nb_2O_5 nanocluster supported by TiO_2 surfaces with different nanocluster sizes (a, b, c, and d). Binding energy vs nanocluster size plots (e). Green, blue, and red balls represent the Nb, Ti, and O atoms, respectively. (For interpretation of the references to colour in this figure legend, the reader is referred to the Web version of this article.)

highest binding energy of about -8.20~eV. Hence, this configuration is considered the most stable one and is chosen for further in-depth analysis. The optimized geometrical structure of these configurations is shown in Fig. 2 (d). Bare TiO2 surfaces have Ti–O bond lengths of 1.84 Å and 1.95 Å. After the deposition of the Nb2O5 nanocluster, the Ti–O bond length was increased to 1.96 Å and 2.00 Å. Also, the isolated Nb2O5 nanocluster has the bond length of 2.01 Å and 1.96 Å; After the nanocluster deposition, the Nb–O bond length was increased to 2.42 Å and 2.01 Å. The increasing bond length of TiO2 and Nb2O5 nanoclusters implicates the superior binding of the adsorbed nanocluster on the TiO2 surfaces.

3.2. Electronic structure analysis

The projected density of states (PDOS) for the $(Nb_2O_5)_4$ nanocluster supported by the TiO_2 surface is shown in Fig. 3. For the case of isolated Nb_2O_5 nanocluster, most of the states from the VBM are made up of O-2p orbitals, while the inner bands have the hybridized states of O-2p and Nb-4d orbitals, and most of the states of CBM are from the Nb-4d orbitals. Also, the calculated electronic structure depicts the semiconductor characteristics of the Nb_2O_5 nanocluster. For the case of Bare TiO_2 Rutile (110) surfaces, VBM is made from O-2p orbitals, and the CBM is made from Ti-3d orbitals; this feature agrees well with our previous results [48,49]. For the case of Nb_2O_5 nanocluster-supported

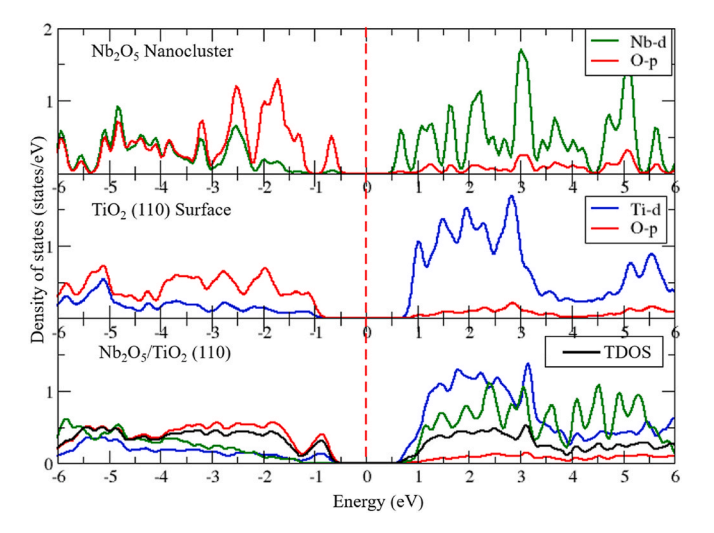


Fig. 3. The projected density of states (PDOS) plots for the most stable configurations of Nb_2O_5 -supported Rutile TiO_2 (110) surfaces. The Fermi level is shifted by 0 eV.

 ${
m TiO_2}$ Rutile (110) surfaces, most of the VBM states are from the O-2p orbitals, and most of the states of CBM are made from Ti-3d orbitals. After 3.5 eV in the conduction bands, it has Nb-4d majority states. After the Nb₂O₅ nanocluster deposition on the surface, there is the generation of small energy states from O-2p orbitals around -1 eV in the VBM. On CBM, the flat band of the Ti-3d orbitals is changed into a dispersed band. The band gap of ${
m TiO_2}$ is also reduced by 0.4 eV after the nanocluster deposition, thus influencing the increased mobility of electron charge carriers in the visible region.

3.3. Charge transfer analysis

The charge density difference plot of Nb_2O_5 nanocluster deposited on TiO_2 Rutile (110) surfaces is shown in Fig. 4. The accumulation and the depletion of charge along the interface can be represented by the yellow and light blue contours. The charge redistribution occurs at the interface, mainly due to the lower coordinated Nb and Ti atoms. This analysis

is further studied by the Bader charge analysis, as shown in Fig. 5. On the ${\rm TiO_2}$ Rutile (110) surfaces, the ${\rm Ti}_{\rm Cc}$ site and ${\rm O}_{\rm 2c}$ site are low-coordinated sites and may be considered as the most active. These active sites bind the ${\rm Nb_2O_5}$ nanoclusters to the surfaces. The ${\rm O}_{\rm 2c}$ sites of ${\rm TiO_2}$ surfaces are considered the most active sites for binding the ${\rm Nb_2O_5}$ nanocluster, which receives a charge of about 0.2e from the ${\rm Nb_2O_5}$ nanocluster. After that, ${\rm Ti}_{\rm 5c}$ sites of the ${\rm TiO_2}$ surface receive 0.08e from the ${\rm Nb_2O_5}$ nanocluster. The ${\rm O}_{\rm 3c}$ sites interact poorly with the ${\rm Nb_2O_5}$ nanocluster and thus receive charges of about 0.04e from the nanocluster.

3.4. NO adsorption on Nb₂O₅/TiO₂

The most active adsorption of the NO molecules is calculated by the adsorption energetics, by analyzing the adsorption at different possible sites. The adsorption energy is calculated based on the formula as mentioned in our previous work [48]. Fig. 6 shows the various adsorption sites of NO molecules on Nb_2O_5 nanocluster-supported TiO_2 surfaces. NO adsorbed at the sideways of the Nb_2O_5 nanocluster (a), NO

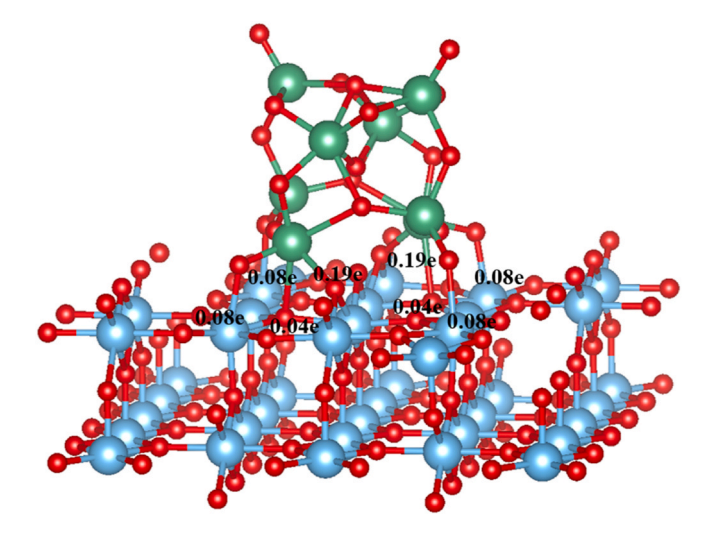


Fig. 5. Bader charge in different active sites at the interface of Nb₂O₅/TiO₂.

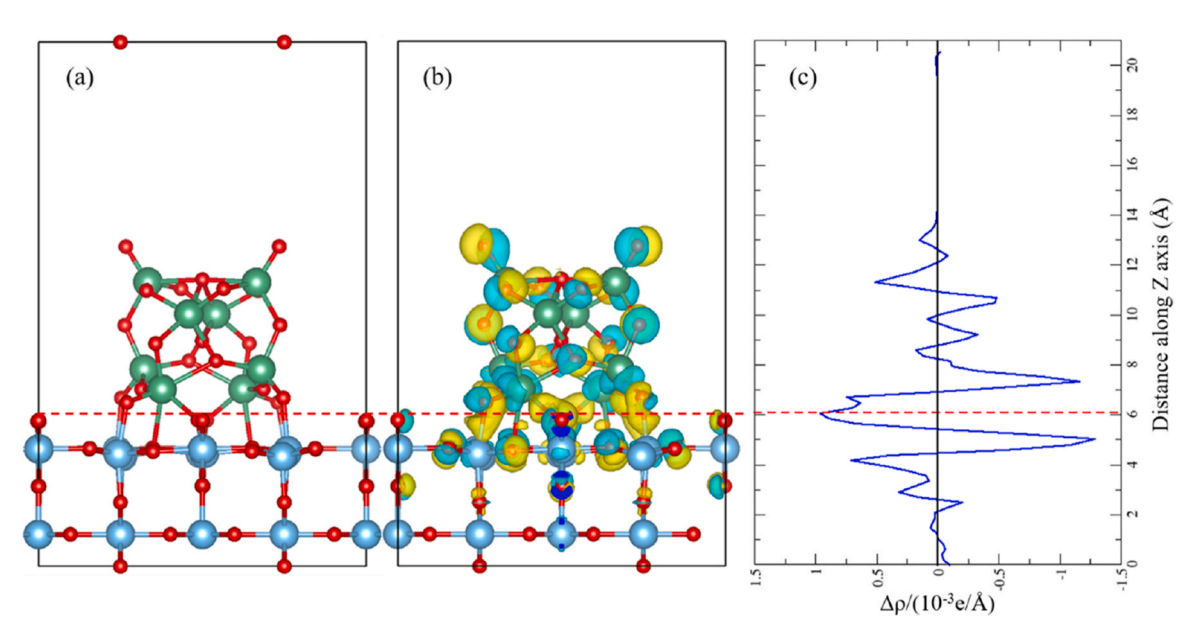


Fig. 4. The optimized structure of the Nb_2O_5/TiO_2 system with its interface shown by red dotted lines (a). The charge density difference isosurface plots with the isovalue of 0.003 e/Å, where yellow and light blue represent the accumulation and depletion, respectively (b), and the planar average charge density difference plots (c). (For interpretation of the references to colour in this figure legend, the reader is referred to the Web version of this article.)

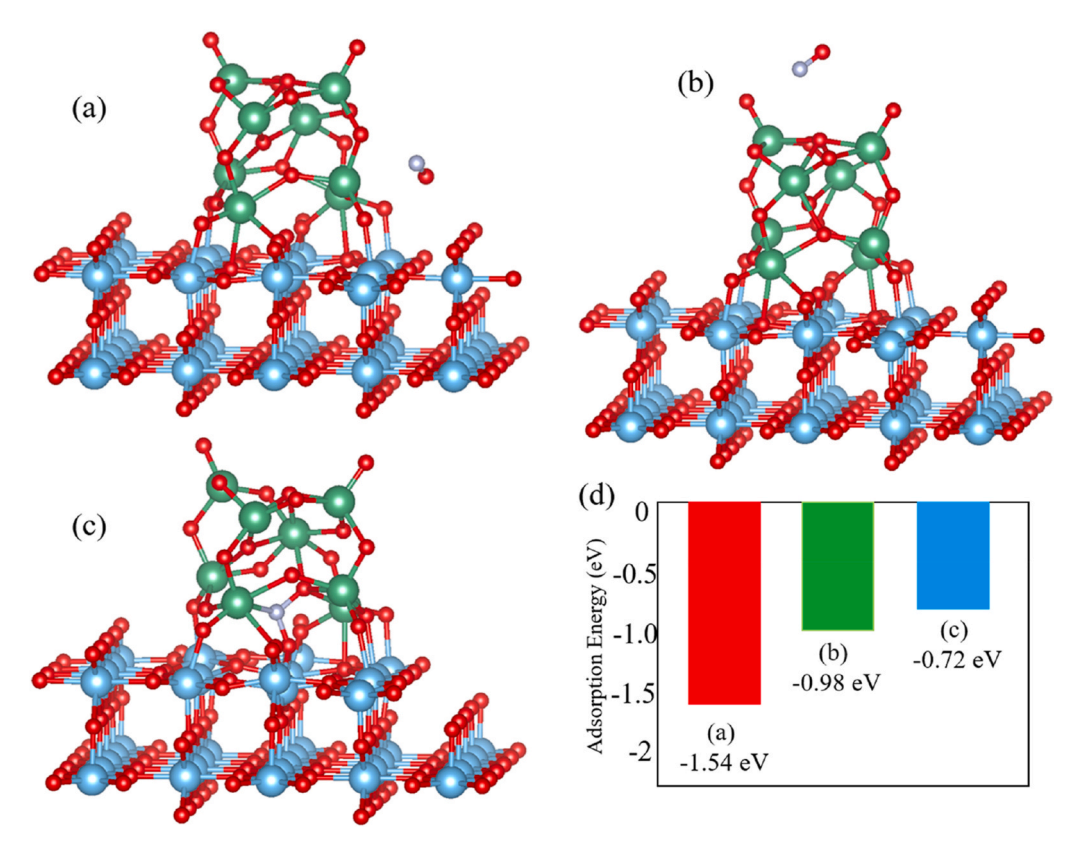


Fig. 6. NO molecule adsorption at various possible adsorption sites of Nb₂O₅/TiO₂ (a, b, c), adsorption energy plots (d). Green, blue, white, and red balls represent the Nb, Ti, N, and O atoms, respectively. (For interpretation of the references to colour in this figure legend, the reader is referred to the Web version of this article.)

adsorbed on the top of the Nb_2O_5 nanocluster (b), and NO adsorbed on the bottom of the Nb_2O_5 nanocluster (c). Among the various adsorption sites, NO adsorbed on the sideways of Nb_2O_5 nanocluster-supported TiO_2 surface has the highest adsorption energy of about -1.54 eV. The NO molecule adsorbed on the sideways is in the exact position where the Nb_2O_5 nanocluster interfaces with the TiO_2 slab. At these adsorption sites, NO molecules are influenced by active adsorption sites such as Nb_{4c} , O_{2c} , and Ti_{5c} of the Nb_2O_5/TiO_2 system. Hence, compared to other adsorption configurations, it has the highest binding energy. Hence, this configuration is considered the most stable one and is chosen for further studies.

3.5. NO reduction reaction

The reaction coordinates profile has been studied for the reduction of Harmful NO molecules into harmless by-products through the following two-step process. The initial step will be converting NO molecules into N_2O and oxygen atoms [50,51]. For this mechanism, the transition state (TS) was calculated by the Climbed Image Nudged Elastic Band method (CI-NEB). Fig. 7 shows the reaction coordinates profile for converting NO molecules into N_2O and oxygen by-products. Initially (IS), two NO molecules co-adsorb on the sideways of Nb_2O_5 nanocluster-supported TiO_2 surfaces. Later, two NO molecules bind together at the transition state with an activation barrier of about 3.40 eV. Then, it attains the intermediate state (IMS)-1 with an exothermic energy of -0.62 eV, with

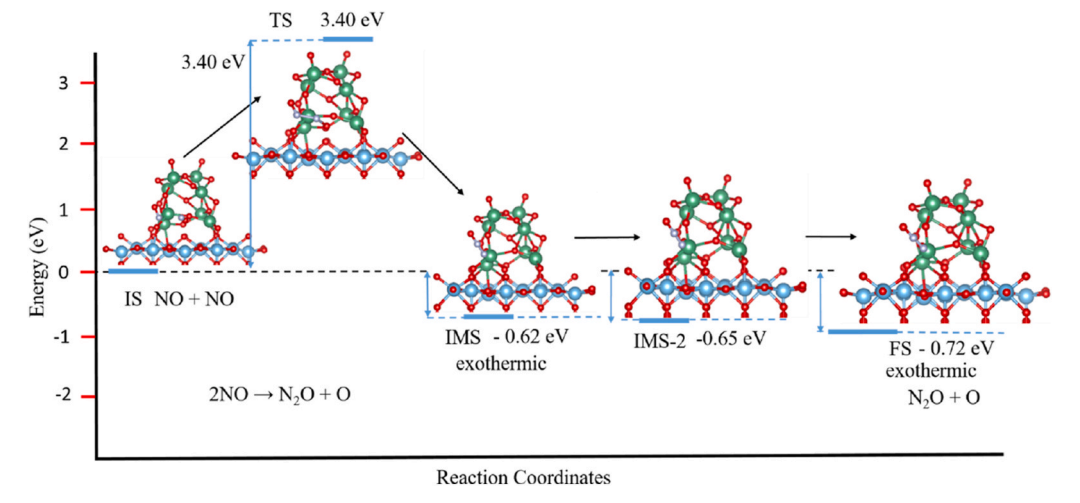


Fig. 7. Reaction coordinates profile for converting NO molecules into N2O and oxygen by-products.

the by-product of N_2O and oxygen atoms. Further, the N_2O molecules adsorbed on the surface and the O ad atoms make a chemical bond with the five-coordinated Ti atoms and four-coordinated Nb atoms at the intermediate state (IMS)-2 with an exothermic energy of -0.65 eV. Later, it attains the final state (FS) with an exothermic energy of about -0.72 eV, with the by-products N_2O and O ad atoms.

Still, the N_2O molecule is considered harmful. Hence, dissociating the N_2O into N and O by-products is necessary for complete environmental purification [50]. The reaction coordinates profile for dissociating N_2O molecules into N and O by-products, is illustrated in Fig. 8. Initially, N_2O is adsorbed on the Ti_{5c} site of the $\text{Ti}O_2$ surface with the O down configuration. Later, the O atom of the N_2O is detached from the molecule and attains the transition state (TS) with activation barriers of about 4.64 eV. Finally, the oxygen atoms make a chemical bond with the five-coordinated Ti and four-coordinated Nb atoms. The N_2 molecules are adsorbed on the $\text{Ti}O_2$ surface at the final state (FS) with an exothermic energy of about -0.17 eV.

3.6. Nb₁₀ nanocluster supported by rutile TiO₂ (110) surface

The calculated structure of the TiO_2 rutile (110) surface-supported Nb_{10} nanocluster is shown in Fig. 9. Initially, the Nb_{10} nanocluster with a different geometry was studied. Different geometries of Nb_{10} nanoclusters, such as pyramidal or tetrahedral (a), spherical (b), and planar (c) geometries, are shown in Fig. S3 in the supplementary materials. Among these Nb_{10} nanoclusters, the tetrahedral geometry has the highest negative cohesive energy of about -9.01 eV and is considered for further studies. Our analysis agreed well with the previous work regarding the tetrahedral nanocluster [52].

Nb $_{10}$ nanocluster with tetrahedral geometry was constructed on the TiO $_2$ surface. For our study, we obtained two layers of TiO $_2$ (110) surface, which is terminated by a 2-coordinated O atom and a 5-coordinated Ti atom. Nb $_{10}$ nanocluster was deposited at the center of the TiO $_2$ surface. The pure Rutile TiO $_2$ (110) surface has an average Ti–O bond length of 1.935 Å. After the deposition of the Nb nanocluster, it increases to 1.943 Å. The Nb nanocluster has an average Nb–Nb bond length of 2.766 Å, and the Nb nanocluster bonds with the 2-coordinated O atom of TiO $_2$ (110) with an average Nb–O bond distance of 2.10 Å. The binding energy of the Nb nanocluster on the TiO $_2$ rutile (110) surface was measured by the following equation (4),

$$E_{B.E} = E_{Nb/surface} - E_{surface} - E_{Nb}$$
 (4)

Where E_{BE} denotes the binding energy of Nb nanocluster on TiO_2 surface, $E_{Nb/surface}$ denotes the total energy of Nb nanocluster deposited on TiO_2 surface, $E_{surface}$ denotes the total energy of TiO_2 rutile (110) surface, and E_{Nb} denotes the total energy of an isolated Nb₁₀ nanocluster.

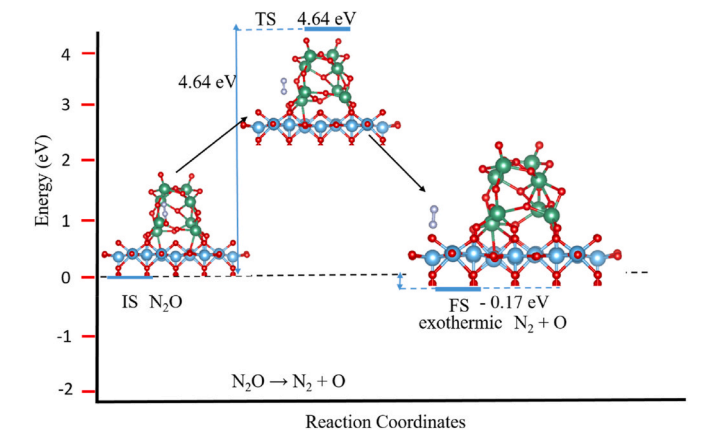


Fig. 8. Reaction coordinates profile for dissociating N_2O molecules into nitrogen and oxygen by-products.

From the above formula, the binding energy of the Nb nanocluster on the ${\rm TiO_2}$ surface was calculated as -6.10 eV. The binding energy is exothermic; hence, the system is thermodynamically stable and can be synthesized experimentally.

The projected density of states (PDOS) of a Nb₁₀ nanocluster deposited on TiO₂ rutile (110) is shown in Fig. 10 (a). From the PDOS, it is found that, in the pure TiO₂ rutile (110), the valence mainly consists of O-2p orbitals, and the conduction band consists of Ti-3d orbitals and shows a perfect semiconducting nature. For the case of an isolated Nb₁₀ nanocluster, the valence band and conduction band overlap; it mainly consists of Nb-4d orbitals. After the deposition of the Nb nanocluster to the TiO2 rutile (110) surface, the Fermi level is shifted towards the conduction band minimum, where we can see the shifting of Ti-3d and O-2p states in the conduction band minimum (CBM) shifted towards the Fermi level. (Fig. 10 (a)). Both occupied states and unoccupied states overlapped and were dominated by Nb-4d states. The Nb nanocluster provides enormous electrons to the TiO2 surface. Hence, due to its n-type nature, the conduction band of TiO₂ was shifted towards the Fermi level. Due to rich electron charge carriers, the band gap region was occupied by Nb-4d states, and the system shows a metallic nature.

The charge flow between the Nb nanocluster and the TiO $_2$ surface is further studied by the Bader charge analysis. Here, Nb nanocluster provides electrons to the TiO $_2$ surface and attains the net charges of +2.71e (Fig. 10 (b)). The distribution of Bader charges on the Nb cluster deposited Rutile TiO $_2$ (110) surface is shown in Fig. 10 (b). It is understood that the atoms in the bottom layer of the Nb $_{10}$ nanocluster, which are in direct contact with the Nb cluster, hold more charges than the other atoms in the nanocluster [52]. The distribution of charges on the Nb nanocluster leads to the creation of an internal electric field along the interface of the TiO $_2$ surface and Nb nanocluster, which is explained below.

The creation of an internal electric field along the interface between the Nb₁₀ nanocluster and TiO₂ surface is further explained by the charge density difference isosurface plot (Fig. 11 (a)) and the planar average charge density difference plot (Figure 11 (c)). Figure 11 (b) shows charge density difference isosurface plots (with the isovalue of 0.003 e/ Å) for the Nb₁₀/TiO₂ system. The yellow and cyan region represents charge accumulation and depletion, respectively. Figure 11 (c) shows the planar average charge density difference plot along the z-direction. Here, the positive values show the charge accumulation and the negative value denotes the charge depletion. The red dotted lines represent the Nb₁₀ nanocluster and TiO₂ surface interface. From the planar average charge density difference plot, the highest negative peak occurs at 7 Å (from Nb₁₀ nanocluster). It is understood that the depletion of charges, i.e., the loss of charges, occurs at the Nb nanocluster. The highest positive peak occurs at 5.5 Å (from the TiO2 surface). It is understood that the accumulation of charges, i.e., the gain of charges, occurs at the TiO2 surface. Hence, it is again confirmed that Nb10 nanocluster provides electrons to the TiO2 surface. From the charge density difference analysis, it is found that the charge accumulation and depletion occur at the interface between the Nb nanocluster and the TiO₂ surface. This charge redistribution leads to the creation of an internal electric field along the Nb nanocluster and TiO2 surface. This creation of an internal electric field will enhance the separation of electron and hole charge carriers, thus eventually increasing the photocatalytic activity of the surface [49,53].

3.7. Oxidation of the NO molecule

Fig. 12 shows the reaction coordinate profile for the oxidation of NO molecules into NO_3^- . Initially, the co-adsorption of NO and O_2 occurred at the interface of the Nb_{10} nanocluster and the TiO_2 surface [54]. The co-adsorbed NO and O_2 come close to each other. Due to the charges provided by the Nb nanocluster, the O_2 molecule is activated and dissociated. For the dissociation of O_2 molecules, it crosses the

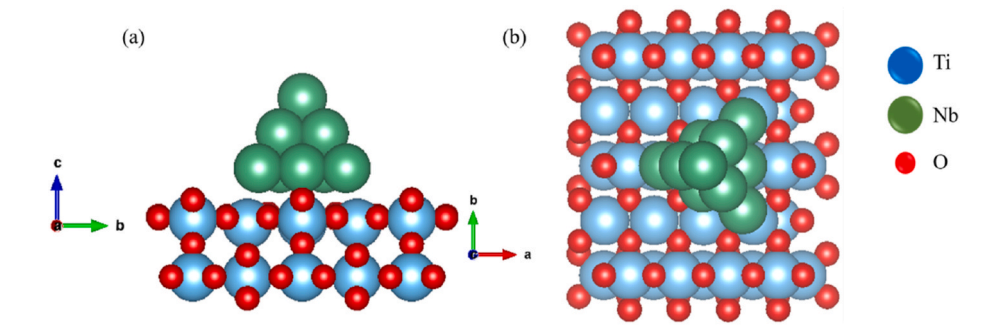


Fig. 9. (a) and (b) show a side view and top view of the optimized structure of the TiO₂ rutile (110) surface-supported Nb nanocluster.

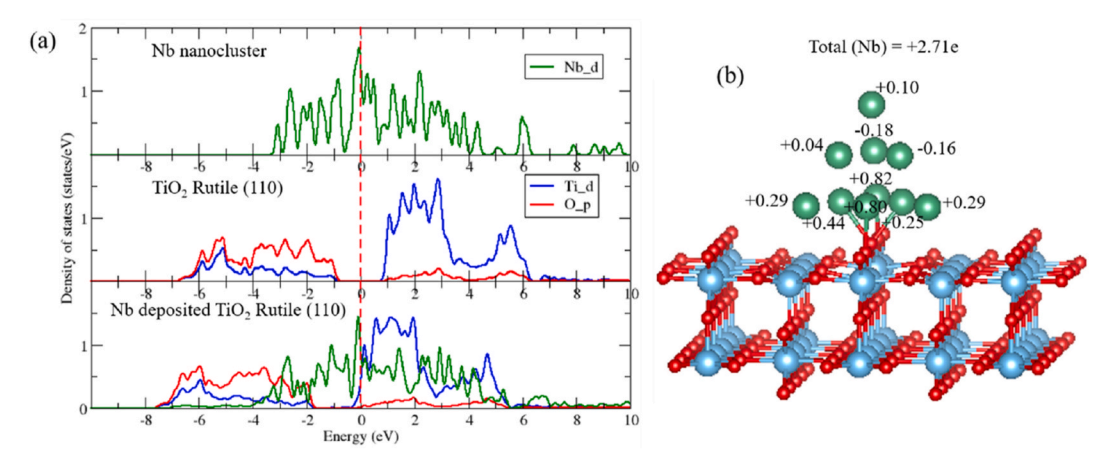


Fig. 10. (a) The projected density of states (PDOS) plots for Nb nanocluster deposited TiO2 rutile (110) surface. (b) Bader charge analysis.

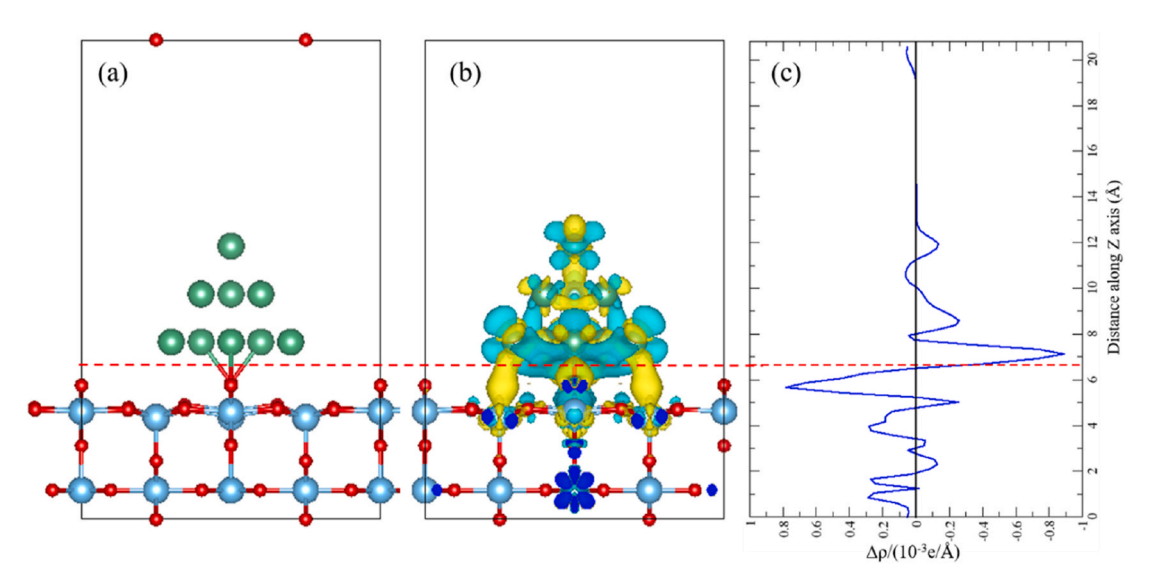


Fig. 11. The optimized structure of the Nb_{10}/TiO_2 , with red dotted lines representing the interface of the structure (a). The charge density difference isosurface plots with the isovalue of 0.003 e/Å. Here, the yellow and light blue regions show charge accumulation and depletion, respectively (b). The planar average charge density difference (c). (For interpretation of the references to colour in this figure legend, the reader is referred to the Web version of this article.)

activation barrier of 3.97 eV, known as the first transition state. The dissociated O atoms make a chemical bond with NO and become NO_2 molecules. After the reaction, it attains the intermediate state with NO_2 molecule configuration and ad O atoms on the TiO_2 surface. The intermediate state is exothermic with an energy of -0.30 eV; hence, this process is thermodynamically favorable. Later, the remaining oxygen atom is attached to the NO_2 molecules and becomes NO_3^- . In this process,

it crosses the activation barrier of 2.05 eV, known as the second transition state. Finally, it attains the final state with an exothermic energy of -2.26 eV; here, the higher negative energy represents the thermodynamic favorability of the reaction.

The PDOS in Fig. 13 shows the initial configurations of co-adsorbed NO and O_2 molecules (a) and the final configurations of NO_3^- formation (b). At the initial states of co-adsorbed NO and O_2 molecules, NO

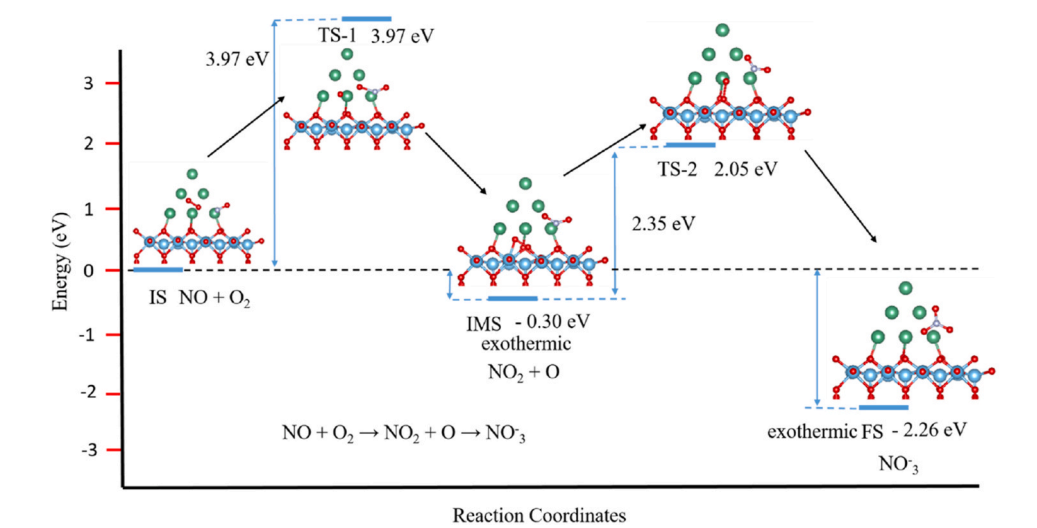


Fig. 12. Reaction coordinates profile for converting NO molecules into NO₃.

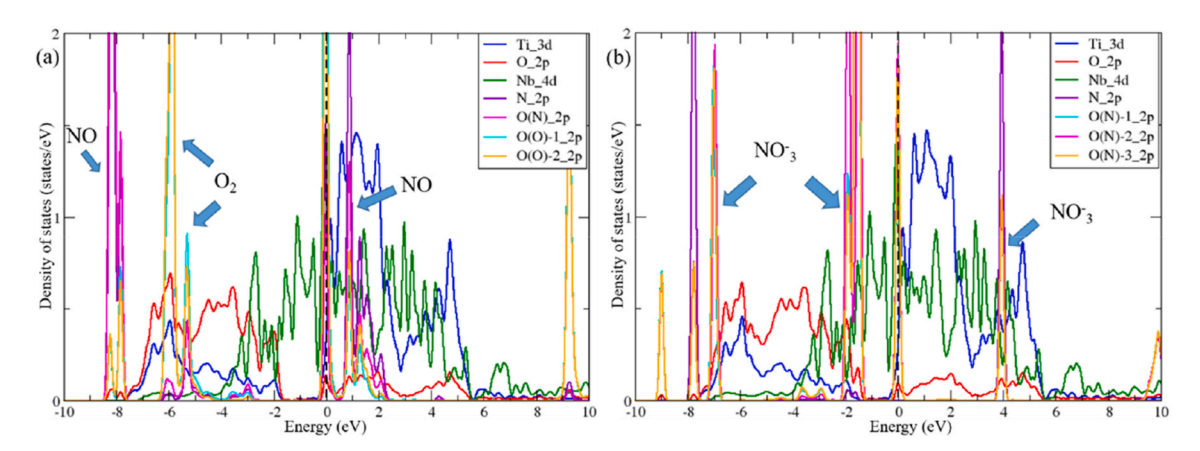


Fig. 13. PDOS for co-adsorbed NO and O_2 at the initial stage of the reaction (a), formation of NO_3^- at the final stage of the reaction (b).

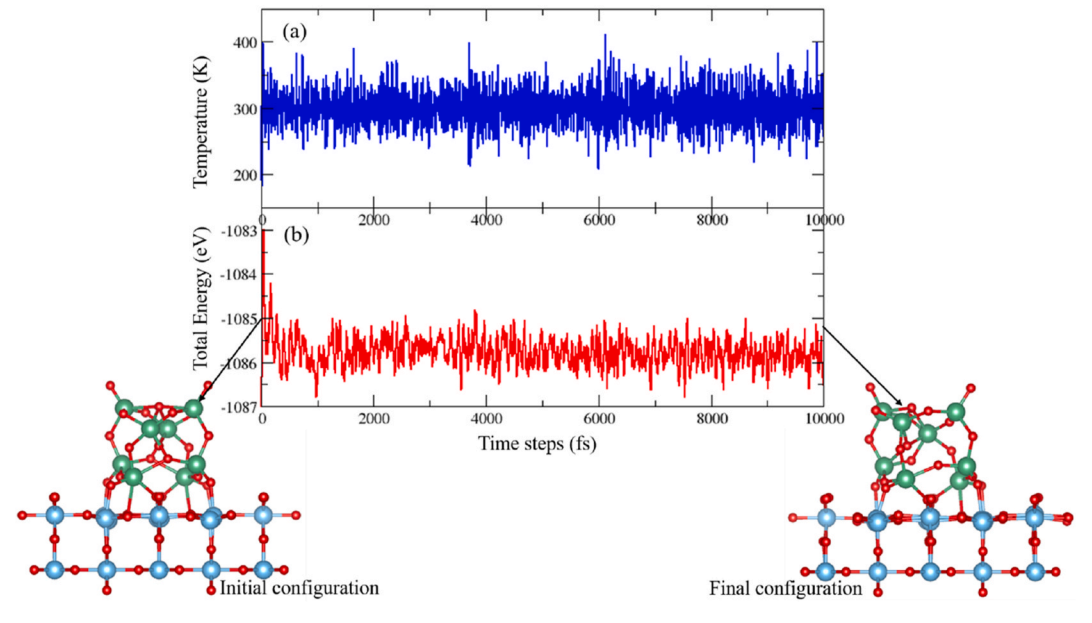


Fig. 14. The AIMD studies for the Nb_2O_5/TiO_2 surfaces, temperature vs time steps plots (a), total energy vs time steps plots (b).

molecules have energy states in the range of around $-8\ eV$ and $1\ eV$, which are hybridized with O-2p of surface oxygen. Co-adsorbed O_2 molecules have states in the energy range around $-6\ eV$, which are also mainly hybridized with surface O-2p orbitals. Overall, both NO and O_2 molecules show distinguished energy states with energy intervals of about $2\ eV$ (Fig. 13 (a)). After the reaction, at the final stage, the formed NO_3^- has states in the energy range of around $-7\ eV$ and $-2\ eV$. NO_3^- is mainly hybridized with O-2p and Nb-4d of the surface. No corresponding states were observed regarding individual NO and O_2 molecules (Fig. 13 (b)). This analysis further confirms the successful formation of NO_3^- from the co-adsorbed NO and O_2 molecules.

3.8. Ab-Initio Molecular Dynamics (AIMD) analysis

To further understand the thermodynamic stability of the nanocluster-supported TiO2 surfaces, Ab-Initio Molecular Dynamics (AIMD) simulation was carried out at 300 K. The thermodynamic and dynamic stability of the system was further studied. Fig. 14 shows the AIMD results for the Nb₂O₅/TiO₂ systems, where the Nb₂O₅ nanocluster supported TiO₂ rutile (110) surfaces is allowed to run over 10,000 fs for 300 K. Figure 14 (a) shows the temperature vs time steps plots. It can be concluded that the temperature is stable around 300 K for the entire 10,000 fs. Therefore, it is understood that the Nb₂O₅/TiO₂ system is thermodynamically stable around room temperature. Figure 14 (b) shows the total energy vs time steps plot, where the total energy of the system is converged around -1086 eV throughout the entire 10,000 fs. Both the initial configuration and the final configuration of the system are more or less the same, with a slight geometrical distortion. Hence, it is understood that the Nb₂O₅/TiO₂ system has dynamic stability at room temperature.

Fig. 15 shows the AIMD results for the Nb₁₀/TiO₂ systems, where the Nb₁₀ nanocluster supported TiO₂ rutile (110) surfaces is allowed to run over 10,000 fs for 300 K. Figure 15 (a) shows the temperature vs time steps plots; it can be concluded that the temperature is stable around 300 K for the entire 10,000 fs. Therefore, it is understood that the Nb₁₀/TiO₂ system is thermodynamically stable around room temperature. Figure 15 (b) shows the total energy vs time steps plot, where the total energy of the system is converged around -915.5 eV throughout the entire 10,000 fs. Both the initial configuration and the final configuration of the system are almost the same. Hence, it is understood that the Nb₁₀/TiO₂ system has dynamic stability at room temperature. From the

AIMD analysis, it is concluded that our proposed nanocluster-supported ${\rm TiO_2}$ surfaces have good thermal stability at room temperature. Thus, it eventually acts as the most stable material to carry out any photocatalytic degradation mechanism.

4. Conclusion

From our DFT-based calculation, we are proposing a possible method for modifying the electronic structure of Rutile TiO2 (110) surfaces with the Nb₂O₅/Nb₁₀ nanocluster. Initially, the growth mechanism of the Nb₂O₅/Nb₁₀ nanocluster on the TiO₂ surface is studied. The favorable geometry and size of the $\mathrm{Nb_2O_5/Nb_{10}}$ nanocluster are studied. The binding energy of Nb₂O₅ nanoclusters on TiO₂ surfaces increases with increasing nanocluster size. The most favorable nanocluster size of Nb₂O₅/Nb₁₀-supported TiO₂ surfaces is chosen for further studies. The Nb₂O₅ nanocluster creates the band gap states along the VBM and CBM of the TiO₂ surfaces, thus helping to achieve visible light absorption. The recombination of electron and hole charge carriers can be greatly suppressed by the Nb₂O₅ nanocluster deposition on the TiO₂ surfaces; these features can be obtained by electronic structure analysis. The charge redistribution between the TiO2 surface and Nb2O5 nanocluster is further studied. The deposition of Nb₁₀ nanoclusters on the TiO₂ surface creates the internal electric field, thus eventually improving the generation of electron and hole charge carriers and suppressing their recombination, thus helping to improve the photocatalytic activity. The thermodynamic stability of the nanocluster-supported TiO2 surfaces is analyzed by AIMD simulation. It is found that both Nb2O5/TiO2 and Nb₁₀/TiO₂ systems have good thermodynamic stability over the entire AIMD simulation at 300 K. The most favorable adsorption sites of the NO molecule on the Nb2O5/TiO2 surface are obtained by the adsorption energetics. It has been known that the sideways of the Nb2O5/TiO2 surface is considered the most favorable adsorption site for NO. The reaction coordinates profile for the conversion of NO into N2O and the latter dissociation of $\mathrm{N}_2\mathrm{O}$ into N and O by-products have been studied. It has been concluded that all the end products at the final state has exothermic energy values, which illustrates that the chemical reactions are thermodynamically favorable. Similarly, the harmful NO molecule into harmless NO₃ conversion mechanism is illustrated with possible reaction coordinate profiles. Our calculations will give the pathway to experimentally build a co-catalyst to act as a novel photocatalyst for environmental pollution reduction.

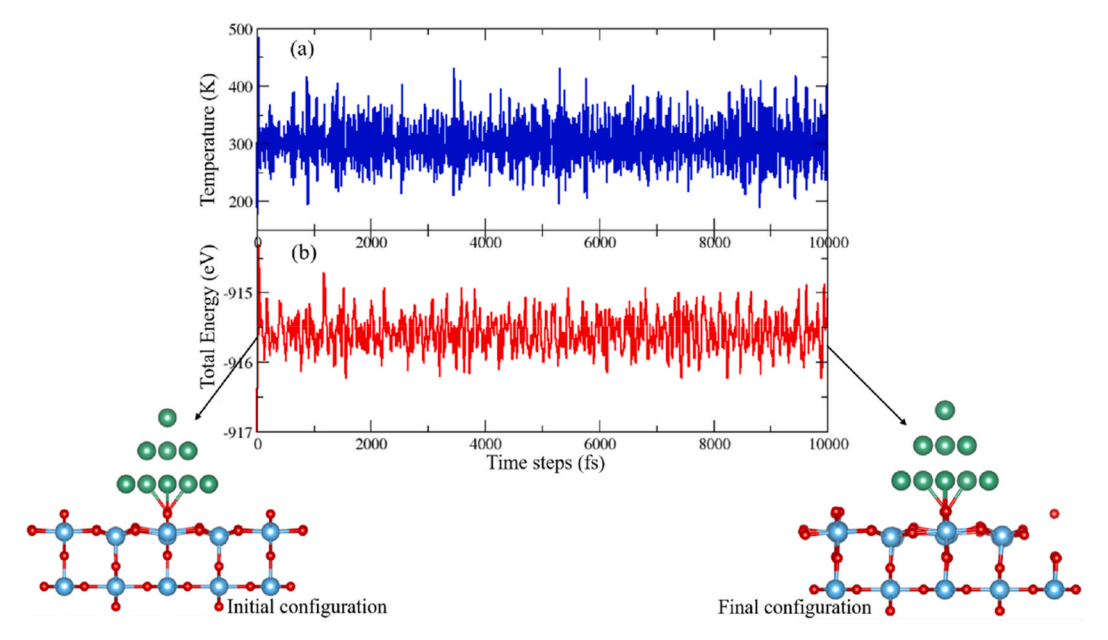


Fig. 15. The AIMD studies for the Nb₁₀/TiO₂ surfaces, temperature vs time steps plots (a), total energy vs time steps plots (b).

From our analysis, the possibility of tuning the TiO₂ semiconductor property by nanocluster surface chemical functionalization is proposed. The recombination of charge carriers is considered a disadvantage for the photocatalytic mechanism. We observed strong evidence for the creation of the internal electric field along the interface of the nanocluster-supported TiO₂ surface. This creation of an internal electric field suppresses the recombination of electron and hole charge carriers. This eventually leads to the enhanced photocatalytic activity. The possible reaction coordinate mechanism is proposed for converting the harmful NO molecules into harmless by-products. The exothermic energy of the Final state of the reaction conveys, the reaction mechanism is thermodynamically stable and naturally favorable. From our results, it is concluded that our proposed novel material, i.e., nanocluster-supported TiO₂ surfaces, will act as a potential co-catalyst for the photocatalytic reduction of harmful NO pollutants. Our findings can directly help the experimentalist to synthesize the Nb-based nanocluster-supported oxide photo catalyst towards the enhanced NO reduction mechanism.

CRediT authorship contribution statement

S. Muthukrishnan: Writing – review & editing, Writing – original draft, Visualization, Validation, Project administration, Investigation, Formal analysis, Data curation, Conceptualization. **R. Vidya:** Writing – review & editing, Validation, Supervision, Software, Resources, Project administration, Methodology, Investigation, Funding acquisition, Conceptualization. **Anja Olafsen Sjåstad:** Writing – review & editing, Supervision, Project administration, Methodology, Funding acquisition, Conceptualization.

Declaration of competing interest

The authors declare that they have no known competing financial interests or personal relationships that could have appeared to influence the work reported in this paper.

Acknowledgments

The authors are grateful to the University of Oslo, Norway, for providing the financial grant through the Indo-Norway project "Oxide Surfaces for Nitrous Oxide Abatement" (CIR/60/INDO-NORWAY/2019). They are also thankful to the Norwegian supercomputer facility, project number NN2875K, for computing time.

Appendix A. Supplementary data

Supplementary data to this article can be found online at https://doi.org/10.1016/j.jpcs.2025.113040.

Data availability

Data will be made available on request.

References

- [1] O. Badr, S.D. Probert, Environmental impacts of atmospheric nitrous oxide, Appl. Energy 44 (3) (1993) 197–231.
- [2] Baukel Charles, Everything you need to know about NOx: controlling and minimizing the pollutant emissions is critical for meeting air quality regulations, Met. Finish. 103 (11) (2005) 18–24.
- [3] T. Boningari, P.G. Smirnoitis, Impact of nitrous oxides on the environment and human health: mn-based materials for NOx abatement, Curr. Opin. Chem. Eng. 13 (4) (2016) 133–141.
- [4] Z. Liu, J. Li, S.I. Woo, H. Hu, Density functional theory studies of NO, and NO2 adsorption on Al2O3 supported SnO2 cluster, Catal. Lett. 143 (9) (2013) 912–918.
- [5] Y. Jin, C. Sun, S. Su, Experimental and theoretical study of the oxidation of air methane over Fe2O3 and CuO, Phys. Chem. Chem. Phys. 17 (25) (2015) 16277–16284.

- [6] M.A. Gomez, V. Pitchon, A. Kiennemann, Pollution by nitrogen oxides: an approach to NOx abatement by using sorbing catalytic materials, Environ. int. 31 (3) (2005) 445–467.
- [7] Z. Yang, T.K. Woo, K. Hermansson, Adsorption of NO on unreduced and reduced CeO2 surfaces: a plane-wave DFT study, Surf. Sci. 600 (22) (2006) 4953–4960.
- [8] Y.H. Lu, H.T. Chen, Computational investigation of NO2 adsorption and reduction on ceria and M-doped CeO2 (111) (M = Mn, Fe) surfaces, J. Phys. Chem. C 118 (19) (2014) 10043–10052.
- [9] S.N. Hong, Y.H. Kye, C.J. Yu, U.G. Jong, G.C. Ri, C.S. Choe, K.H. Kim, Ju M. Han, Ab initio thermodynamic study of SnO2 (110) surfaces in an O2 and NO environment: a fundamental understanding of the gas sensing mechanism for NO and NO2, Phys. Chem. Chem. Phys. 18 (46) (2016) 31566–31578.
- [10] C. Fan, S. Su, J. Xiang, L. Sun, S. Hu, Q. Zhao, P. Wang, S. Lei, Density functional studies of adsorption properties of NO and NH3 over CuO/gama Al2O3 catalyst, Appl. Surf. Sci. 261 (15) (2012) 659–664.
- [11] H. Liu, H. Liu, Y. Feng, J. Shao, Y. Chen, Z.L. Wang, H. Li, X. Chen, Z. Bian, Self-cleaning triboelectric nanogenerator based on TiO₂ photocatalysis, Nano Energy 70 (2) (2020) 104499.
- [12] M. Ramamoorthy, D. Vanderbilt, First-principles calculations of the energetics of stoichiometric Ti02 surfaces, Phys. Rev. B 49 (1994) 16721–16727.
- [13] S.W. Verbruggen, TiO2 photocatalysis for the degradation of pollutants in the gas phase: from morphological design to plasmonic enhancement, J. Photochem. Photobiol., A C 24 (3) (2015) 64–82.
- [14] A. Cabrera-Reina, A.B. Martínez-Piernas, Y. Bertakis, N.P. Xekoukoulotakis, A. Agüera, J.A. Sanchez Perez, TiO2 photocatalysis under natural solar radiation for the degradation of the carbapenem antibiotics imipenem and meropenem in aqueous solutions at pilot plant scale, Water Res. 166 (2) (2019) 115037.
- [15] M. Park, Y.T. Ko, M. Ji, J.S. Cho, D.H. Wang, Y.-I. Lee, Facile self-assembly-based fabrication of a polyvinylidene fluoride nanofiber membrane with immobilized titanium dioxide nanoparticles for dye wastewater treatment, J. Clean. Prod. 378 (2) (2022) 134506.
- [16] Z. Qi, Y. Miyazaki, M. Sugasawa, Y. Yang, N. Negishi, Antibacterial silver-loaded TiO2 ceramic photocatalyst for water purification, J. Water Process Eng. 50 (3) (2022) 103225
- [17] M.R. Al-Mamun, S. Kader, M.S. Islam, M.Z.H. Khan, Photocatalytic activity improvement and application of UV-TiO2 photocatalysis in textile wastewater treatment: a review, J. Environ. Chem. Eng. 7 (21) (2019) 103248.
- [18] J. Han, E.-K. Jang, M.-R. Ki, R.G. Son, S. Kim, Y. Choe, S.P. Pack, S. Chung, pH-responsive phototherapeutic poly(acrylic acid)-calcium phosphate passivated TiO2 nanoparticle-based drug delivery system for cancer treatment applications, J. Ind. Eng. Chem. 112 (5) (2022) 258–270.
- [19] S. Muthukrishnan, R. Vidya, Anja Olafsen sjåstad, band gap engineering of anatase TiO2 by ambipolar doping: a first principles study, Mater. Chem. Phys. 299 (2023) 127467, https://doi.org/10.1016/j.matchemphys.2023.127467, 0254-0584.
- [20] E. Gyorgy, G. Socol, E. Axente, I.N. Mihailescu, C. Ducu, S. Ciuca, Anatase phase TiO2 thin films obtained by pulsed laser deposition for gas sensing applications, Appl. Surf. Sci. 247 (10) (2005) 429–433.
- [21] A. Orendorz, A. Brodyanski, J. Losch, L.H. Bai, Z.H. Chen, Y.K. Le, C. Ziegler, H. Gnaser, Phase transformation and particle growth in nanocrystalline anatase TiO2 films analyzed by X-ray diffraction and Raman spectroscopy, Surf. Sci. 601 (3) (2007) 4390–4394.
- [22] Pelaez M, N.T. Nolan, S.C. Pillai, M.K. Seery, P. Falaras, A.G. Kontos, P.S.M. Dunlop, J.W.J. Hamilton, J.A. Byrne, K. Oshea, M.H. Entezari, D.D. Dionysiou, A review on the visible light active titanium dioxide photocatalysts for environmental applications, Appl. Catal. B Environ., vol. 125, no. 3, pp. 331–349.
- [23] E.M. Bayan, L.E. Pustovaya, M.G. Volkova, Recent advances in TiO2-based materials for photocatalytic degradation of antibiotics in aqueous systems, Environ. Technol. Innovat. 24 (3) (2021) 101822.
- [24] Haocheng Wu, Wentao Jiang, Liyi Shi, Rengui Li, Lei Huang, Can Li, Photo-assisted sequential assembling of uniform metal nanoclusters on semiconductor support, iScience 25 (1) (2022) 103572, https://doi.org/10.1016/j.isci.2021.103572. ISSN 2589-0042.
- [25] X. Chen, C. Burda, The electronic origin of the visible-light absorption properties of C-, N- and S-Doped TiO2 nanomaterials, J. Am. Chem. Soc. 130 (15) (2008) 5018–5019
- [26] I. Tamiolakis, I.N. Lykakis, G.S. Armatas, Mesoporous, CdS-sensitized TiO2 nanoparticle assemblies with enhanced photocatalytic properties: selective aerobic oxidation of benzyl alcohols, Catal. Today 250 (6) (2015) 180–186.
- [27] V. Boppana, B.R. Lobo, SnOx–ZnGa2O4 photocatalysts with enhanced visible light activity, ACS Catal. 1 (8) (2011) 923–928.
- [28] C. Liane, F. Riemke, V. Goetzke, M.L. Moreira, C.W. Raubach, E. Longo, S. cava, Facile preparation of Nb₂O₅/TiO2 heterostructure for photocatalytic application, Chem. Phys. Impact 2 (2) (2022) 100079.
- [29] Q. Jin, M. Fujishima, H. Tada, Visible-light-active iron oxide modified anatase titanium(iv) dioxide, J. Phys. Chem. C 115 (5) (2011) 6478–6483.
- [30] R. Stephen, Michael Nolan, Activation of Water on MnOx –nanocluster modified rutile (110) and anatase (101) TiO2 and the role of cation reduction, Front. Chem. 7 (67) (2019) 1–12.
- [31] C. Liane, F.C. Riemke, N.F. de Andrade Neto, A. de A.G. Santiago, T. J. Siebeneichler, N.L.V. Carreno, M.L. Moreira, C.W. Raubach, S. Cava, Influence of Nb₂O₅ crystal structure on photocatalytic efficiency, Chem. Phys. Lett. 764 (3) (2021) 138271.
- [32] R.R.M. Silva, J.A. Oliveira, L.A.M. Ruotolo, A.L.A. Faria, C. Ribeiro, F.G. E. Nogueira, Unveiling the role of peroxo groups in Nb₂O₅ photocatalytic efficiency under visible light, Mater. Lett. 273 (4) (2020) 127915.

- [33] C. Liane, V. Goetzke, S.R. Almeida, E.C. Moreira, M.M. Ferrer, P.L.G. Jardim, M. L. Moreira, C.W. Raubach, S. Cava, Photocatalytic degradation of rhodamine B using Nb2O5 synthesized with different niobium precursors: factorial design of experiments, Ceram. Int. 47 (4) (2021) 20570–20578.
- [34] Bhanupriya Boruah, R. Gupta, J.M. Modak, G. Madras, Enhanced photocatalysis and bacterial inhibition in Nb2O5: via versatile doping with metals (Sr, Y, Zr, and Ag): a critical assessment, Nanoscale Adv. 1 (7) (2019) 2748–2760.
- [35] J. Yan, G. Wu, N. Guan, L. Li, Nb2O5/TiO2 heterojunctions: synthesis strategy and photocatalytic activity, Appl. Catal. B Environ. 152 (4) (2014) 280–288.
- [36] S.Y. Mendiola-Alvarez, J. Arana, J.M. Dona Rodríguez, A. Hern Mendez-Ramírez, G. Turnes Palomino, C. Palomino Cabello, L. Hinojosa-Reyes, Comparison of photocatalytic activity of αFe2O3-TiO2/P on the removal of pollutants on liquid and gaseous phase, J. Environ. Chem. Eng. 9 (1) (2021) 104828.
- [37] R. Vagner, de Mendonça, W. Avansi, R. Arenal, C. Ribeiro, A building blocks strategy for preparing photo catalytically active anatase TiO2/rutile SnO2 heterostructures by hydrothermal annealing, J. Colloid Interface Sci. 505 (5) (2017) 454-459
- [38] P. Haowei, L. Jingbo, L. Shu-Shen, X. Jian-Bai, First-principles study of the electronic structures and magnetic properties of 3d transition metal doped anatase TiO2, J. Phys. Condens. Matter 20 (12) (2008) 125207.
- [39] Y. He, O. Dulub, H. Cheng, A. Selloni, U. Diebold, Evidence for the predominance of subsurface defects on reduced anatase TiO2(101), Phys. Rev. Lett. 102 (10–13) (2009) 106105.
- [40] M.A. Henderson, W.S. Epling, C.H.F. Peden, C.L. Perkins, Insights into photoexcited electron scavenging processes on TiO2 obtained from studies of the reaction of O2 with OH groups adsorbed at electronic defects on TiO2(110), J. Phys. Chem. B 107 (2) (2003) 534–545.
- [41] A. García, Nick Papior, Arsalan Akhtar, Siesta: recent developments and applications, J. Chem. Phys. 152 (20) (2020) 204108.
- [42] J.M. Soler, Emilio Artacho, Julian D. Gale, Alberto Garcia, Javier Junquera, Pablo Ordejon, The SIESTA method for ab initio order- N materials simulation, J. Phys. Condens. Matter 14 (11) (2022) 2745.
- [43] J.P. Perdew, K. Burke, M. Ernzerhof, Generalized gradient approximation made simple, Phys. Rev. Lett. 77 (18) (1996) 3865–3868.

- [44] N. Troullier, J.L. Martins, Efficient pseudopotentials for plane-wave calculations physical review B 43 (3) (1991) 1993–2006.
- [45] W. Tang, E. Sanville, G. Henkelman, A grid-based Bader analysis algorithm without lattice bias, J. Phys. Condens. Matter 21 (2009) 084204.
- [46] G. Henkelman, B.P. Uberuaaga, H. Jonsson, A climbing image nudged elastic band method for finding saddle points and minimum energy paths, J. Chem. Phys. 113 (22) (2000) 9901–9904.
- [47] K. Momma, F. Izumi, VESTA: a three-dimensional visualization system for electronic and structural analysis, J. Appl. Crystallogr. 41 (3) (2008) 653–658.
- [48] S. Muthukrishnan, R. Vidya, Anja Olafsen sjåstad, Illustrating the surface chemistry of nitrogen oxides (NO_x) adsorbed on rutile TiO₂ (110) with the aid of STM and AIMD simulation, Catal. Sci. Technol. 15 (2025) 1850–1864.
- [49] S. Muthukrishnan, R. Vidya, Anja olafsen sjåstad, exploring the electronic structure and interfacial phenomena of pseudomorphic rutile (110) heterostructure: an Ab initio study, ACS Appl. Eng. Mater. (2025), https://doi.org/10.1021/ acsaenm 5c00313
- [50] H. Koga, K. Tada, A. Hayashi, et al., High NO_x reduction activity of an ultrathin zirconia film covering a Cu surface: a DFT study, Catal. Lett. 147 (2017) 1827–1833, https://doi.org/10.1007/s10562-017-2086-5.
- [51] H. Koga, K. Tada, A. Hayashi, Y. Ato, M. Okumura, Potential of titania-covered Ag catalysts for NOx reduction: a DFT study, Chemical Letters 46 (4) (2017) 456–459.
- [52] H. Koga, K. Tada, M. Okumura, DFT study of CO oxidation catalyzed by Au/TiO2, Activity of small clusters, e-Journal of surface science and Nanotechnology 13 (5) (2015) 129–134.
- [53] M.R. Ashwin Kishore, K. Larsson, P. Ravindran, Two-dimensional CdX/C2N (X = S, Se) heterostructures as potential photocatalysts for water splitting: a DFT study, ACS Omega 5 (37) (2020) 23762–23768, https://doi.org/10.1021/acsomega.0c02804.
- [54] Nishant Biswakarma, Dikshita Dowerah, Satyajit Dey Baruah, Plaban Jyoti Sarma, Kishor Gour Nand, Chandra Deka Ramesh, Catalytic oxidation of NO to NO2 on pure and doped AunPt3-n (n=0-3) clusters: a DFT perspective, Mol. Catal. 515 (2021) 111910, https://doi.org/10.1016/j.mcat.2021.111910, 2468-8231.